

A study on the working mechanism of internal pressure of super-large cooling towers based on two-way coupling between wind and rain

Shitang Ke^{*1}, Wenlin Yu^{2a} and Yaojun Ge^{3b}

¹Department of Civil Engineering, Nanjing University of Aeronautics and Astronautics, 29 Yuda Road, Nanjing 210016, China

²Jiangsu Power Design Institute Co., LTD, China Energy Engineering Group, 58-3 Suyuan Road, Nanjing 211102, China

³State Key Laboratory for Disaster Reduction in Civil Engineering, Tongji University, 1239 Siping Road, Shanghai 200092, China

(Received September 2, 2017, Revised February 27, 2019, Accepted March 1, 2019)

Abstract. In the current code design, the use of a uniform internal pressure coefficient of cooling towers as internal suction cannot reflect the 3D characteristics of flow field inside the tower body with different ventilation rate of shutters. Moreover, extreme weather such as heavy rain also has a direct impact on aerodynamic force on the internal surface and changes the turbulence effect of pulsating wind. In this study, the world's tallest cooling tower under construction, which stands 210m, is taken as the research object. The algorithm for two-way coupling between wind and rain is adopted. Simulation of wind field and raindrops is performed iteratively using continuous phase and discrete phase models, respectively, under the general principles of computational fluid dynamics (CFD). Firstly, the rule of influence of 9 combinations of wind speed and rainfall intensity on the volume of wind-driven rain, additional action force of raindrops and equivalent internal pressure coefficient of the tower body is analyzed. The combination of wind velocity and rainfall intensity that is most unfavorable to the cooling tower in terms of distribution of internal pressure coefficient is identified. On this basis, the wind/rain loads, distribution of aerodynamic force and working mechanism of internal pressures of the cooling tower under the most unfavorable working condition are compared between the four ventilation rates of shutters (0%, 15%, 30% and 100%). The results show that the amount of raindrops captured by the internal surface of the tower decreases as the wind velocity increases, and increases along with the rainfall intensity and ventilation rate of the shutters. The maximum value of rain-induced pressure coefficient is 0.013. The research findings lay the basis for determining the precise values of internal surface loads of cooling tower under extreme weather conditions.

Keywords: super-large cooling tower; two-way coupling between wind and rain; CFD; combination of wind velocity and rainfall intensity; pressure distribution on the internal surface

1. Introduction

Along with the extensive applications of large-capacity high-parameter generator set, an increasing number of (super) large cooling towers, one of the core structures of thermal and nuclear power plants, have been constructed (Wu 1996). Super-large cooling tower is a typical wind-sensitive structure, and wind load is the control load in structural internal force design. Compared with ordinary cooling towers, super-large cooling towers have more complex distribution patterns of aerodynamic force and flow field on the internal surface (Ke *et al.* 2015). Super-large cooling towers are subjected to the joint action of strong wind and heavy rain under extreme weather. The trajectories of raindrops will slant under the joint action of wind force and gravity. The raindrops will enter through the open top of cooling tower, making high-velocity impact on

the inner wall of the tower body. This will significantly change the distribution of aerodynamic force on the internal surface. In addition, heavy rain can cause a substantial deterioration of turbulence effect related to the pulsating wind when there is no rain (Xin *et al.* 2011, Li and Bai 2008). The air movement pattern inside the tower is made more complex by different ventilation rate of shutters at the tower base, which further changes in the trajectory of raindrops, additional load and internal pressures. Therefore, it is of high theoretical and engineering value to study the working mechanism of flow field and aerodynamic force inside the super-large cooling tower under the joint action of wind and rain.

Researches concerning wind load of super-large cooling towers mainly focus on stochastic behaviors of single wind load (Zhang *et al.* 2013), extreme wind pressure distribution (Chen *et al.* 2016), static interference effects (Niemann and Kopper 1998) and dynamic interference effect (Ke and Ge 2014). Chinese code for design (GB/T 50102-2014 2014) provides the calculation formula of standard value of internal suction for super-large cooling towers, with the value of internal pressure coefficient being -0.5. Germany code (VGB-R610Ue 2005) also assumes that the internal pressure coefficient remains constant along the height and circumferential directions, with the value of internal pressure coefficient taken as -0.5. However, Shen *et al.*

*Corresponding author, Ph.D.

E-mail: keshitang@163.com

^a Postgraduate, Engineer

E-mail: nuaayuwenlin@163.com

^b Ph.D. Professor

E-mail: yaojunge@tongji.edu.cn

(2011) simulated wind loads on internal surface of the cooling tower under the effect of cold-heat air circulation system and external wind field by using the $k-\varepsilon$ turbulence model and multiphase flow model. Their calculation indicated significant changes of internal pressure coefficient along height and latitude directions. Ke *et al.* (2015) found that different ventilation rates of shutters produced a considerable impact on pressure distribution and flow field characteristics on the internal surface of the cooling tower. Zou *et al.* (2015) analyzed 3D effects of wind pressure distribution in internal surface of tower body under different ventilation rates (100% and 30%) by rigid pressure test, finding that non-uniform distribution of wind pressure on internal surface along height and circumferential directions. The above researches determine the values of wind pressure on the internal surface of large cooling towers. But the aerodynamic performance of the internal surface of super-large cooling towers under different combinations of wind velocity and rainfall intensity is rarely discussed. Few studies (Ke *et al.* 2018, Ke *et al.* 2015) focus on the influence of different ventilation rate of shutters on the working mechanism of internal pressure.

In addition, some researches (Blocken *et al.* 2010, Goudarzi and Sabbagh-Yazdi 2011, Xin *et al.* 2012, Bennett *et al.* 2011, Wang and Xu 2010, Fu *et al.* 2016, Zhang *et al.* 2010, Wang *et al.* 2013) concerning wind-rain combined effect mainly focus on bridge cable, low-rise buildings, wind turbine and power transmission tower. They only consider effects of wind-induced rainfall, but overlook reaction of rain to wind. Currently, very few researchers consider the influence of wind-driven rain on the aerodynamic performance of the internal surface of large cooling towers.

Addressing this problem, we take the world's tallest cooling tower under construction, which stands 210m, as the research object. Numerical simulation of wind field surrounding the cooling tower is performed using CFD technique under different wind velocities. Discrete phase model (DPM) is incorporated into the stabilized wind flow and different rainfall intensities are input. Then simultaneous iteration of raindrops and wind field is performed based on the algorithm for two-way coupling between wind and rain, and this method significantly improves the accuracy of the simulation. The 3D distribution of wind pressures on the internal surface of the cooling tower is discussed under the joint action of wind and rain. The rule of influence of different wind velocity and rainfall intensity on the volume of wind-driven raindrops, additional load imposed by raindrops and equivalent internal pressure is extracted. Wind/rain loads, distribution of aerodynamic force, and working mechanism of internal pressure on the internal surface of super-large cooling towers are compared under different ventilation rate of shutters (0%, 15%, 30% and 100%). Finally, values of equivalent internal pressure coefficient are provided for different segments of the tower under different ventilation rates of shutters.

2. Two-way coupling method between wind and rain

2.1 Rainfall intensity

Rainfall intensity (R) is defined as flux of rainfall

Table 1 Two classifications of rainfall intensity

Grade of rainfall intensity	Light rain	Moderate rain	Heavy rain	Rainstorm	Downpour			
					Weak	Moderate	Strong	Extreme
Daily (mm/24h)	10	25	50	100				200
Hourly (mm/h)	2.5	8	16	32	64	100	200	709.2

passing through a horizontal plane in unit time, usually in the unit of mm/h. Compared with mean precipitation in 12h and 24h used in meteorology, hourly precipitation is a more intuitive measure of the influence of instantaneous rainfall intensity during extreme weather events on structure performance. Therefore, hourly precipitation is a meaningful indicator in the engineering field. Table 1 shows two classification of rainfall intensity based on different sampling time. It can be seen from the table that the measurements of the same rainfall event differ greatly under different classifications. Here hourly rainfall intensity is used.

2.2 Raindrop size spectrum

Raindrops are usually considered as spheres, and raindrop size distribution is characterized using approximate diameter of the raindrops. Raindrop size distribution varies with time and space, and raindrop size function is known as raindrop size distribution, which approximately obeys a negative exponential distribution. The commonly used models to describe raindrop size distribution (Mcfarquhar and List 2010, Hodson 1986, Mcfarquhar 2016) include Best's size distribution, Marshall-Palmer distribution and Gamma raindrop size distribution. We adopt Marshall-Palmer distribution, as expressed in Eq. (1):

$$n(D) = N_0 e^{-\lambda D} \quad (1)$$

where D is the raindrop diameter, in the unit of mm; $n(D)$ is the raindrop number concentration spectrum of raindrops of different diameters; N_0 is the raindrop number concentration, usually taken as a constant equivalent to $8000 \text{ (m}^{-3} \cdot \text{mm}^{-1}\text{)}$; λ is the scale parameter, given by Eq. (2):

$$\lambda = 4.1 \times R^{-0.21} \quad (2)$$

where R is rainfall intensity (mm/h).

2.3 Terminal velocity of raindrops

The descending velocity of raindrops increases continuously under the action of gravitation and the air resistances increases as well. Raindrops finally fall at a uniform velocity, which is the terminal velocity of raindrops. According to the research (Gunn and Kinzer 1949), all raindrops will reach the terminal velocity after a fall distance $\geq 20 \text{ m}$.

According to some relevant literatures (Marshall and Palmer 1948, Rigby *et al.* 2010), raindrops smaller than 2mm are considered as spheres as they fall. However, air resistance will induce large deformation of raindrops over

2mm in diameter. The following empirical formula is proposed to estimate the terminal velocity of raindrops in the vertical direction (Eq. (3)):

$$v(D) = 9.1549\left(\frac{D}{2}\right)^{0.5} - 2.6549 + 2.5342e^{-3.727\left(\frac{D}{2}\right)^{0.5}} - 0.389\left(\frac{D}{2}\right)^{2.18} \quad (3)$$

where $v(D)$ is terminal velocity of raindrop with a diameter of D in the vertical direction (m/s).

2.4 Solving the two-way coupling between wind and rain

During the downpour, the volume fraction of raindrops in air is far smaller than 10% (Liu *et al.* 2017, Douvi and Margaris 2012). Here DMP model is used for raindrop simulation. It is the second phase integrated into the continuous phase after the wind field stabilizes for solving two-way coupling between wind and rain. The trajectory of a discrete phase particle can be predicted by integrating the force balance on the raindrop, which is written in a Lagrangian reference frame. Based on ANSYS FLUENT 13.0 (ANSYS Inc. 2011), the dynamic equilibrium equation of motion of raindrops in a wind field is expressed as follows:

$$\frac{d\vec{u}_p}{dt} = F_D(\vec{u} - \vec{u}_p) + \frac{\vec{g}(\rho_p - \rho)}{\rho_p} + \vec{F} \quad (4)$$

where \vec{u}_p is the velocity of discrete phase (particle); \vec{u} is the velocity of continuous phase (fluid); $F_D(\vec{u} - \vec{u}_p)$ is the drag force related to the mass of a unit particle; ρ_p and ρ are the densities of particle and fluid, respectively; \vec{F} is the interaction force between the discrete phase and continuous phase, where

$$F_D = \frac{18\mu}{\rho_p D_p^2} \frac{C_D Re}{24} \quad (5)$$

where μ is the coefficient of viscosity for the fluid; D_p is the particle diameter; Re is the relative Reynolds number, given by

$$Re = \frac{\rho D_p |u_p - u|}{\mu} \quad (6)$$

Considering the influence of raindrops as the discrete phase, the basic governing equation for wind as the continuous phase is expressed as

$$\frac{\partial \rho}{\partial t} + \nabla \cdot (\rho \vec{u}) = S_m \quad (7)$$

$$\frac{\partial}{\partial t} (\rho \vec{u}) + \nabla \cdot (\rho \vec{u} \vec{u}) = -\nabla p + \nabla \cdot (\vec{\tau}) + \rho \vec{g} + \vec{F} \quad (8)$$

where S_m is the mass of the second discrete phase after integrating the continuous phase; p is the pressure; $\vec{\tau}$ is the stress tensor; $\rho \vec{g}$ is gravity, and its stress tensor is given by

$$\vec{\tau} = \mu[(\nabla \vec{u} + \nabla \vec{u}^T) - \frac{2}{3} \nabla \cdot \vec{u} I] \quad (9)$$

where I is unit tensor. The second term on the right side of the equation represents volumetric expansion.

2.5 Particle-wall collision equation

The impact of raindrops on the wall surface of tower cylinder obeys the law of conservation of momentum. The key to solving the impact force lies in solving the time of collision. Evaporation, splash and rupture of raindrops during impact are neglected. The interaction between the raindrops and structure obeys Newton's second law of motion. In the momentum theorem,

$$\int_0^\tau f(t) dt + \int_{v_s}^0 m dv = 0 \quad (10)$$

where $f(t)$ is the vector of impact force of a single raindrop, in the unit of N; v is the raindrop velocity vector.

The impact force imposed by the raindrop within unit time $F(\tau)$ is given by

$$F(\tau) = \frac{1}{\tau} \int_0^\tau f(t) dt = \frac{mv_s}{\tau} \quad (11)$$

The falling raindrops are considered as spheres:

$$F(\tau) = \frac{mv_s}{\tau} = \frac{1}{6\tau} \rho \pi D_p^3 v_s \quad (12)$$

Diameter of raindrops is generally smaller than 6mm and the final horizontal velocity before the impact is relatively high. To simplify the computation, the impact time of raindrops is set as the process of raindrops passing through their radius at the final speed (Chen 2009, Yang and Lou 2011), and the impact time τ is determined as:

$$\tau = \frac{D_p}{2v_s} \quad (13)$$

The impact force imposed by the raindrop to the structure is simplified as


$$F(\tau) = \frac{1}{6\tau} \rho \pi D_p^3 v_s = \frac{2v_s}{6d_p} \rho \pi D_p^3 v_s = \frac{1}{3} \rho \pi D_p^2 v_s^2 \quad (14)$$

3. An overview of the project and configuration of working conditions

3.1 An overview of the project

The super-large cooling tower under construction stands 210m and has a zero meter diameter of 180m. The height of throat is 157.5m and the diameter is 110m. The height of air inlet is 32.5m and the diameter is 159m. The thickness of tower body increases exponentially, with the smallest thickness occurring at the throat, where the wall thickness is 0.37m. The maximum wall thickness occurs at the lower ring, which is 2.0m. The tower is built with 52 pairs of X-shaped pillars, which are connected to the circular foundation. The X-shaped pillars have a rectangular cross-section measuring 1.8m×1.2m. The circular foundation is a cast-in-situ reinforced concrete structure with a width of

Table 2 Structural dimension and schematic of the super large cooling tower

Component	Height/m	Middle surface radius/m	Wall thickness of tower body/m	Concrete grade	Overall schematic
Tower body	32.50	80.50	2.00	C40	
	67.24	70.48	0.46		
	102.57	61.80	0.40		
	138.46	56.08	0.38		
	157.50	55.19	0.37		
	174.79	55.77	0.38		
	208.51	58.05	0.50		
Pillar	52 pairs of X-shaped pillars with 1.8m×1.2m rectangular cross section			C45	
Circular foundation	12.0m wide and 2.5m high			C35	

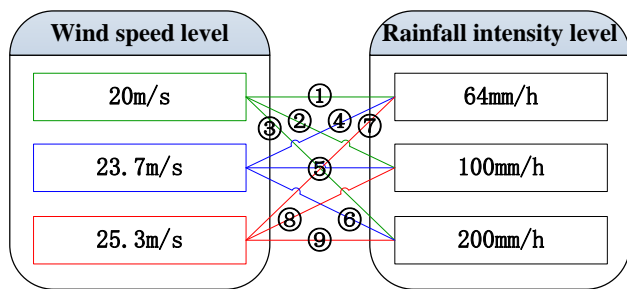


Fig. 1 Different combinations of wind and rain parameters

12.0 m and a height of 2.5 m. Table 2 shows the structural dimension and schematic of the super large cooling tower.

3.2 Different combinations of wind and rain parameters

The tower lies in Binchang County, Shanxi Province, and belongs to the B-type landform (GB 50009-2012 2012). The aerodynamic performance on the internal surface of the cooling tower is compared under three combinations of wind velocity and rainfall intensity. Small wind, moderate wind and strong wind are defined based on the maximum wind velocity with a return period of 10, 50 and 100 years, respectively. Rainfall intensity is simulated as that of rain storm, and three levels of rainfall intensity are considered: weak, moderate and strong rain storms. Thus 9 combinations are calculated, as shown in Fig. 1.

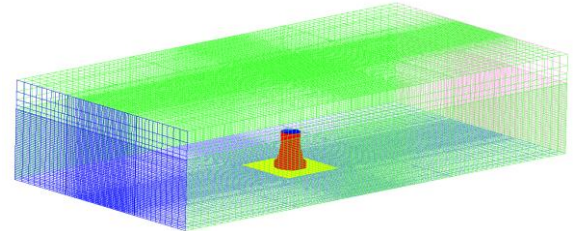
4. Numerical simulation through two-way coupling between wind and rain

4.1 Building a wind-rain field model

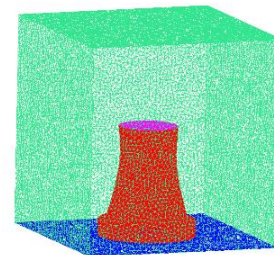
To make sure that the cooling tower is located in the precipitation area and to allow for complete development of wake flow, the entire computational domain has an along-wind length of 3000 m, an across-wind width of 1500 m, and a height of 600 m. The origin of the coordinate system is located at the center of the tower base, with the X-axis pointing to the along-wind direction. Giving consideration to both computational efficiency and precision, the

Table 3 Grid quality and pressure coefficients on windward side at throat of the tower under different gridding schemes

Gridding schemes	I	II	III	IV	V
Total number of grids	1.1 million	4.5 million	10.4 million	18.3 million	28.6 million
Minimum Orthogonal Quality of grids	0.13	0.36	0.53	0.61	0.64
Grid skewness	0.95	0.87	0.82	0.74	0.71
Wind pressure coefficients on windward side	0.92	0.88	0.85	0.80	0.79



(a) Overall meshing



(b) Local meshing

Fig. 2 Schematic of overall and local meshing

computational domain is divided into local and peripheral wind-rain fields during meshing. The local wind-rain field consists of the cooling tower model, and it is divided using non-structured meshes. The peripheral wind-rain field has a more regular shape and divided using structured meshes. Before determining the computational grids, the grid independence verification was performed firstly. Grid quality and pressure coefficients on windward side at throat height of the tower body under different gridding schemes

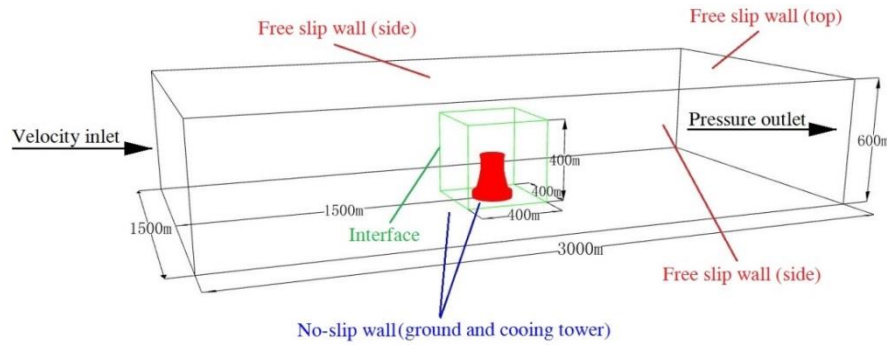


Fig. 3 Schematic of computational domain and boundary conditions

are shown in Table 3. The Minimum Orthogonal Quality of grids shall be larger than 0.1 and it is best to be higher than 0.2. No negative volume is allowed. The grid skewness shall be lower than 0.95 and it is suggested to be lower than 0.9 (Jiang 2008). It can be seen from Table 3 that with the increase of grid number, grid quality, grid skewness and wind pressure coefficient on the windward side converge gradually. There's no significant difference on grid quality and calculation results between the gridding scheme 18.3 million and the gridding scheme of 28.6 million. By combining calculation accuracy and efficiency, the gridding scheme of 18.3 million was applied in this paper. Here both the mesh number and quality satisfy the requirement. Fig. 2 shows the schematic of the entire computational domain and meshing of the model.

The inlet of the computational domain is set as velocity inlet, and the outlet as pressure outlet. The two side walls and top surface are symmetry boundaries whose property is free slip wall. The tower and ground are set as walls whose property is no-slip wall. The overlap surfaces between the local and peripheral computational domains are interfaces. The computational domain of wind-rain field and its boundary conditions are shown in Fig. 3.

4.2 Wind-rain field coupling

The application of two-way coupling between wind and rain and discrete phase trajectory tracking to such structures with extra high Reynolds number raises a very high requirement on computer memory. Here, numerical calculation is undertaken by our large calculation server at the high-performance calculation center for aerodynamic design of wind turbines, as shown in Fig. 4. Intel(R) Xeon(R) CPU E5-2650 v3 @ 2.30GHz 2.30GHz is used. The memory installed is as high as 256GB, and 64-bit operating system is used. When simulating rain, parallel processing is used and more than 16 processes are better. In addition, there can't be too many rainfall points and tries numbers of discrete random walk model.

3D single-precision, segregated solver is used. The flow field velocity is the absolute velocity. Air model is equivalent to ideal incompressible fluid. $k-\omega$ shear-stress transport (SST) model is used as the computational model. The wind profile model with a power exponent of 0.15 is used for the inlet of the computational domain. The wind velocities at the height of 10m above the ground are set as



(a) Calculation center



(b) Calculation server

Fig. 4 High-performance calculation center for aerodynamic design of wind turbines and calculation server

three baseline wind velocities in section 2.2. The flow field is solved by the coupling between wind velocity and pressure via the SIMPLEC algorithm. The convection term is solved in its second-order form. Correction for mesh inclination is configured to increase the computational accuracy of mixed meshes. The residual error of the governing equation is set to 1×10^{-6} . Then the wind field is initialized and iterative computation proceeds. Fig. 5 shows the comparison of simulated and theoretical values of mean wind velocity and turbulence intensity profile. The results indicate that the mean wind velocity and turbulence intensity profile agree well with the theoretical values. The simulated wind field satisfies the engineering requirements.

After the solution of wind field stabilizes, discrete phase is integrated for iterative computation of wind-rain field coupling. Six raindrop diameters within the range of 1.0-6.0mm are used to simulate precipitation with continuous distribution of raindrop diameter (Table 4). The occupancy of number and volume of raindrops with varying diameters

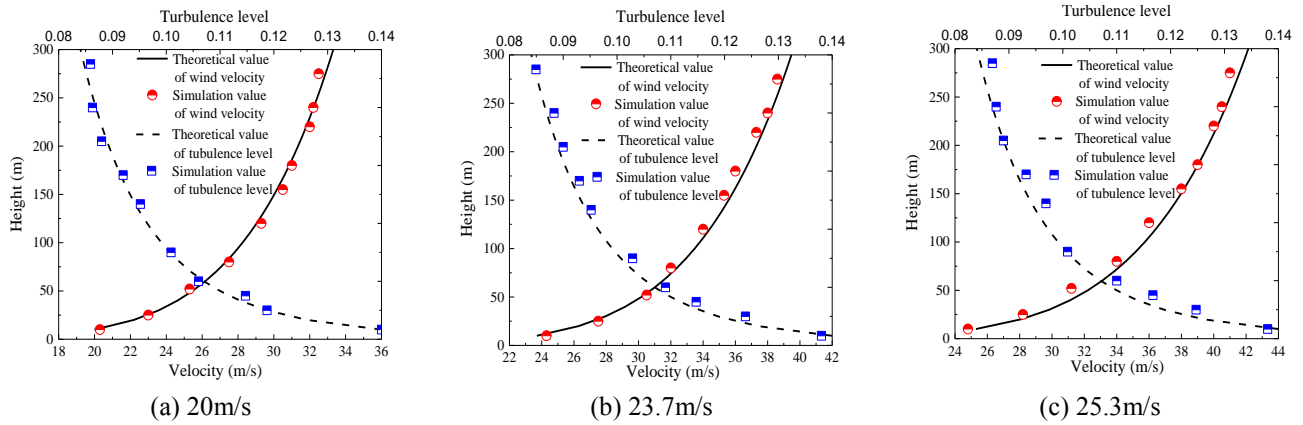


Fig. 5 Wind velocity and turbulence intensity profiles

Table 4 Different raindrop diameters

Raindrop diameter (mm)	1	2	3	4	5	6
Control range (mm)	0~1.5	1.5~2.5	2.5~3.5	3.5~4.5	4.5~5.5	5.5~6

is determined from the Marshall-Palmer distribution described in section 2.2. Then raindrops are released on a horizontal plane, with a velocity of 0. Under the action of wind force, raindrops finally achieve a velocity comparable to the horizontal wind velocity at the same position. The release velocity in the vertical direction is -5 m/s. The raindrops will reach the terminal velocity under the joint action of gravity and resistance after falling for a sufficiently large distance.

The internal surface boundary condition of the cooling tower is set to capture (trap). In the coupling calculation of wind and rain, the number of rain drops can be displayed intelligently on the inner surface. The boundary of outer surface of the structure and other walls are set to escape (escape). When the raindrop meets the boundary, it stops the orbit calculation and records the basic information of the impact moment.

After the iteration is over, the result of continuous phase flow field and the raindrop data captured on the internal surface of the cooling tower are output. The impact of raindrops on the internal surface of the cooling tower is calculated, and the distribution pattern of equivalent internal pressure coefficient under the joint action of wind and rain is discussed.

4.3 Validation

The mean wind pressure coefficients of throat of the cooling tower under the three wind velocities are compared with the values in relevant codes (DL/T 5339-2006 2006, VGB-R 610Ue 2005), and also with the measured curves (Sun and Zhou 1983), as shown in Fig. 6. It can be seen that the angles corresponding to the extreme values of negative wind pressure and the separation points at the throat under the three wind velocities are consistent with the values in the codes and the measured curve. The negative pressure in

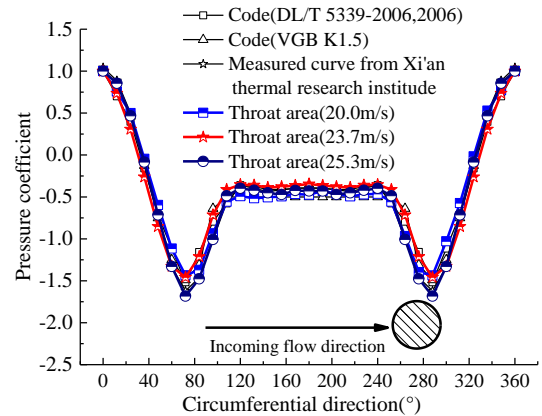


Fig. 6 Comparison of wind pressure coefficients of the throat under the three wind velocities with the values in relevant codes and with the measured curves

the leeward region is slightly higher than the value in Chinese code and the measured value, but smaller than the value in the German code. The values at other angles are basically consistent with those in the codes and the measurements. Taken together, the result of numerical simulation in this paper is considered effective and stable.

5. Analysis under different combinations of wind and rain parameters

5.1 Wind field analysis

Figs. 7-8 are the vorticity contours and 3D wind velocity streamlines under the three baseline wind velocity v_0 before integrating the raindrops, respectively. The following is observed:

(1) Because of neckdown at the throat of the hyperbolic cooling tower, the ascending airflow inside the tower body is hindered to some extent. Moreover, the incoming flow accelerates at the tower top, which changes the direction of part of the ascending air flow. The backward movement of the airflow produces large vortices at the throat.

(2) As the wind velocity increases, the airflow inside the tower body begins to move at an accelerating speed. Consequently, the vortex shedding phenomenon becomes more apparent, and the wind velocity streamlines are denser.

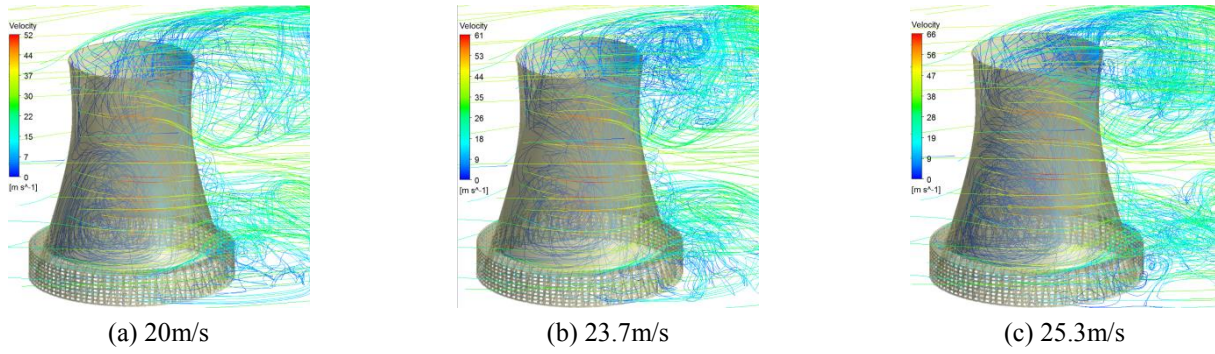


Fig. 7 3D wind velocity streamlines under different wind velocities

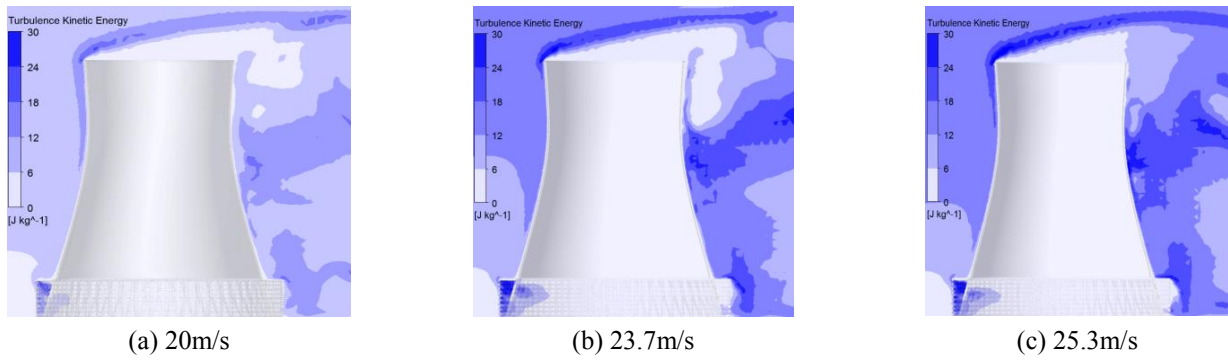


Fig. 8 Turbulence kinetic energy of the cooling tower under different wind velocities

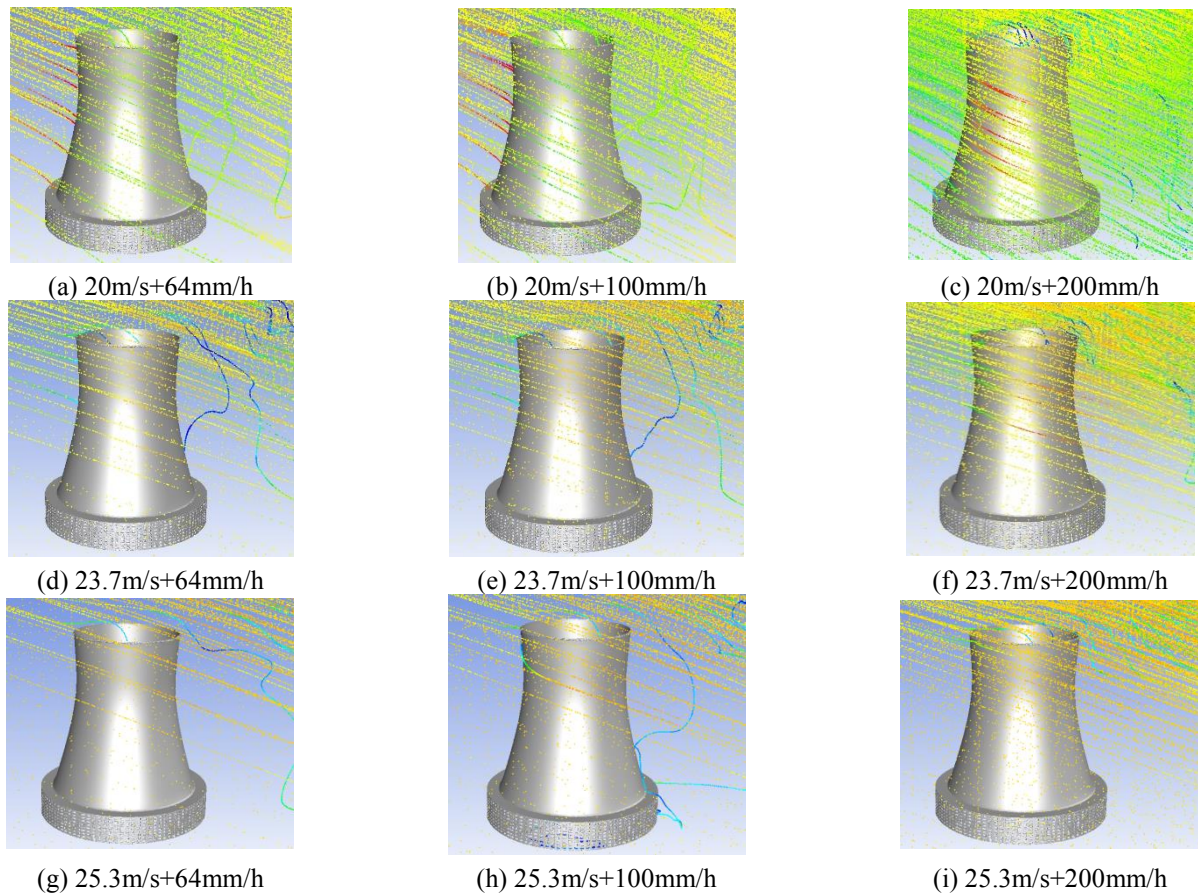


Fig. 9 Raindrop trajectories in the coupled wind and rain fields

As the ascending airflow and incoming flow interact with each other to a greater extent at the tower top, the vortex

shedding phenomenon in the leeward region becomes more significant.

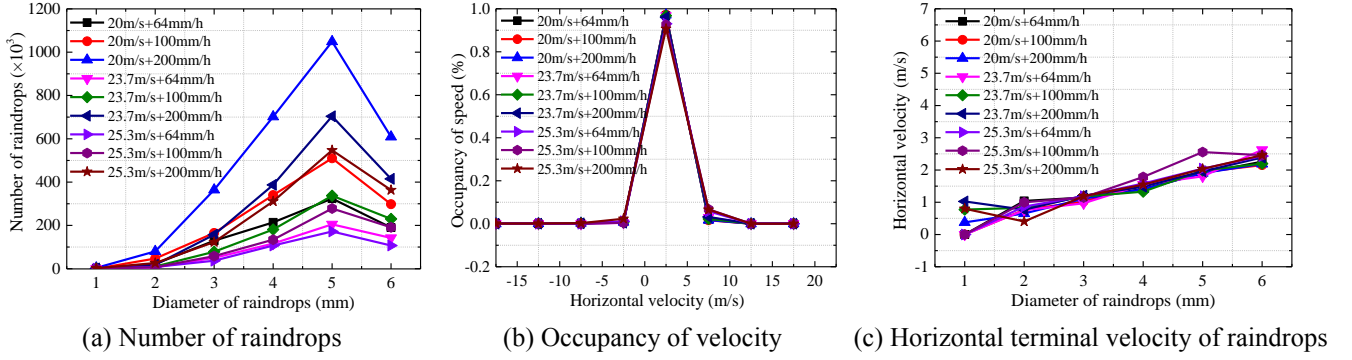


Fig. 10 Distribution of number and terminal velocity of raindrops with different diameters under different working conditions

(3) As the wind velocity increases, the turbulence kinetic energy increases as well, especially in the middle and lower part of the leeward region of the tower body. Peaks mainly occur in the top of the windward region in the tower body, leeward region in the throat, inside the windward region and outside the leeward region of the shutters.

5.2 Rain field analysis

Raindrop trajectories are tracked based on the resultant velocity of particles. Fig. 9 is the schematic of raindrop trajectories in the coupled wind and rain fields under 9 working conditions. The level of raindrop density is subject to proportional coarsening. The following is observed from Fig. 9:

(1) Raindrops fall obliquely rather than vertically due to the action of wind. The inclination of raindrop trajectories becomes greater with the increase of wind velocity, but it is weakly affected by rainfall intensity.

(2) In front of the upper part of the cooling tower, the raindrops enter the tower body via the air outlet under the joint action of wind force, gravity and air resistance. They hit the leeward region in the middle and upper part of the internal surface of the cooling tower at a large speed. The higher the rainfall intensity, the more raindrops collected on the internal wall surface.

(3) As the wind velocity increases, the horizontal force acting on the raindrops increases significantly and propels the along-wind movement of raindrops at an accelerating rate. A large amount of raindrops slide over the tower top and move towards the back of the tower body. As a result, the number of raindrops entering the cooling tower decreases dramatically. This phenomenon becomes more significant as the upward force imposed by airflow at the air outlet on the raindrops is greater under higher wind velocity.

Airflow movement changes suddenly near the wall surface due to structural barrier and air outlet effect. However, the change of horizontal velocity of raindrops lags behind as compared with the change of wind velocity due to inertial effect. Therefore, the instantaneous velocity of raindrops hitting the wall surface is no longer equivalent to horizontal wind velocity. Fig. 10 shows the comparison of number, impact velocity and occupancy of velocity of raindrops with different diameters under 9 working conditions. The following is observed from Fig. 10:

(1) The amount of raindrops collected on the internal surface decreases as the wind velocity increases, and increases along with the rainfall intensity. Different working conditions are ranked in a decreasing order of the number of raindrops collected on the internal surface: working condition 3 > working condition 6 > working condition 9 > working condition 2 > working condition 1 > working condition 5 > working condition 8 > working condition 4 > working condition 7.

(2) The occupancy and values of horizontal raindrop velocity are basically consistent under different working conditions. The raindrops hit the internal surface of the tower body at a speed of 0-5m/s, and the corresponding occupancy is as high as 95%.

(3) The mean horizontal raindrop velocities on the internal surface are far smaller than the baseline wind velocities under different working conditions. The values vary from 1 to 3m/s, and the impact velocity increases as the raindrop becomes larger.

5.3 Analysis of equivalent internal pressure coefficient

For quantitative comparison of pressure distribution on tower surface under different working conditions, the equivalent internal pressure coefficient was defined, which is expressed in the Eqs. (15)-(17).

$$C_{p_{ei}} = C_{p_{wi}} + C_{p_{ri}} \quad (15)$$

$$C_{p_{ri}} = \frac{P_{ri}}{P_{wz_0}} \quad (16)$$

$$P_{ri} = \frac{F_{ri}}{S_i} \quad (17)$$

where $C_{p_{ei}}$ is the equivalent internal pressure coefficient at monitoring point i . $C_{p_{wi}}$ is the wind-induced internal pressure coefficient at the monitoring point. $C_{p_{ri}}$ is the rain-induced internal pressure coefficient. P_{ri} is rain pressure. P_{wz_0} is the wind pressure at the reference height. In this paper, the reference height of monitoring point was set at the equivalent height in far front of the monitoring point. F_{ri} is rain loads and S_i is the calculation area.

Fig. 11 shows the 3D distribution of wind-induced internal pressure coefficient on the internal surface of the

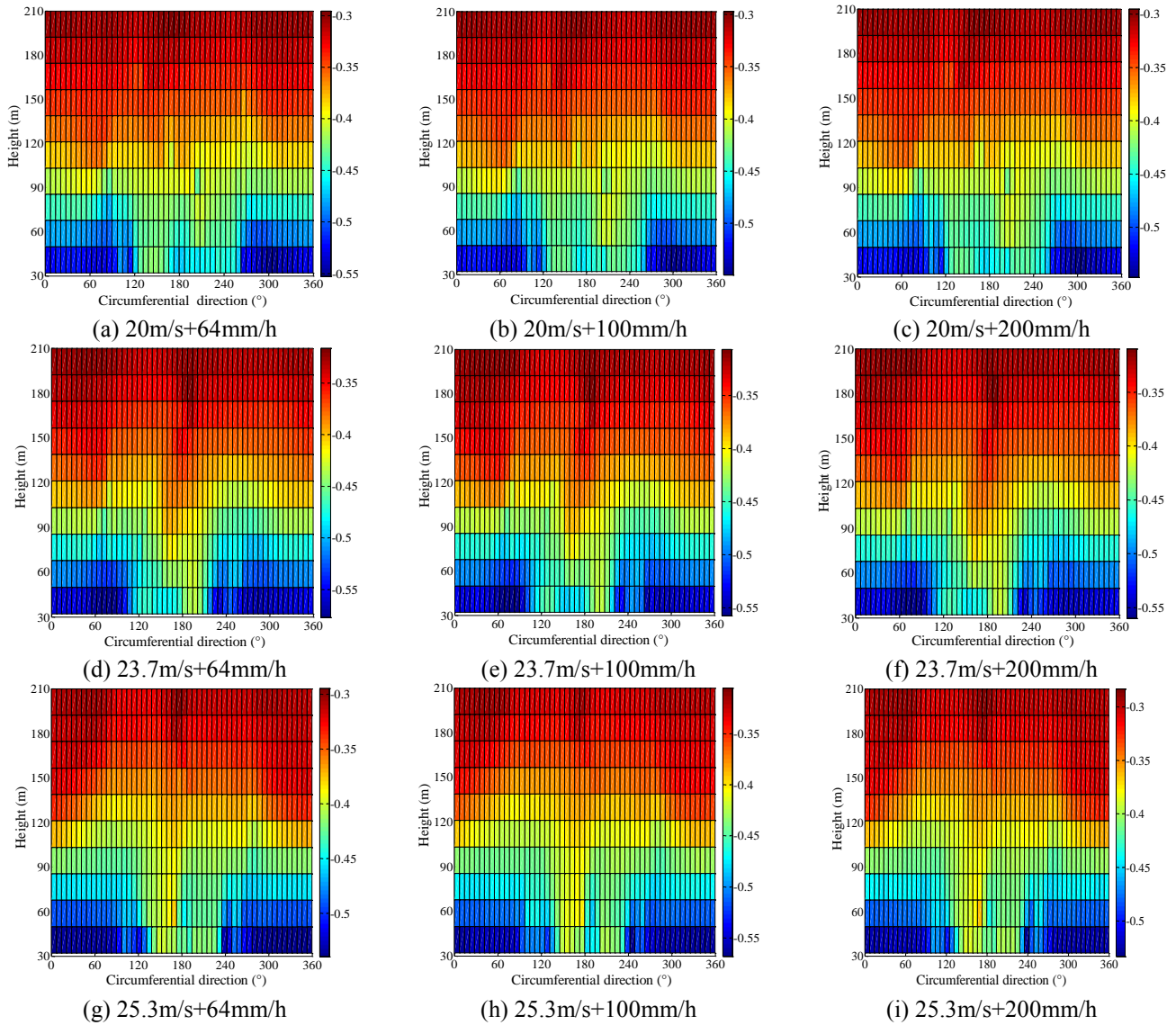


Fig. 11 3D distribution of wind-induced internal pressure coefficient under different working conditions

cooling tower under different working conditions. It can be seen that the values along the circumferential and meridional directions vary under different working conditions. But the values are generally symmetrical about the wind axis. Due to the influence from the airflow passing through the shutters, the wind-induced internal pressure coefficients at the tower base jump violently. The absolute values of the leeward region are much smaller than those in other regions.

The rain loads on the internal surface of the cooling tower are computed using Eq. (14) under nine working conditions. The ratios of rain to wind load on the internal surface at different heights (H is tower height 210m) are shown in Tables 5-7. Different shades of color in the Table indicate different values of the ratio.

(1) The rain load on the internal surface of the tower increases with height. No raindrops are collected on the internal surface of the tower below the height of $0.69H$ (145m). The majority of the rain load is concentrated in $0.90-1.0H$ (189-210m), accounting for about 95%.

(2) The ratio of rain to wind load is extremely small under different heights, the maximum being only 3.655‰, which occurs at the height of $0.90-1.0H$ under working condition 3.

(3) The rain load increases with rainfall intensity under each wind velocity. An increase in wind velocity under a fixed rainfall intensity will cause a reduction in rain load on the internal surface.

Distributions of aerodynamic force on the internal surface of the tower are compared quantitatively under nine working conditions, that is, in terms of equivalent internal pressure coefficient. The following procedures are followed: (1) The rain loads at each monitoring point on the internal surface are converted to rain pressures; (2) The ratio of rain pressure to wind pressure at the monitoring point is the rain-induced internal pressure coefficient; (3) The vector sum of rain-induced internal pressure coefficient and wind-induced internal pressure coefficient is the equivalent internal pressure coefficient that considers the joint action of wind and rain.

Table 5 Eigenvalues of wind and rain loads on internal surface at different heights from conditions 1 to 3

Height	20m/s+64mm/h			20m/s+100mm/h			20m/s+200mm/h		
	Rain load (N)	Wind load (kN)	Ratio (‰)	Rain load (N)	Wind load (kN)	Ratio (‰)	Rain load (N)	Wind load (kN)	Ratio (‰)
0.00~0.69H	0	-9331.4	0	0	-9298.6	0	0	-9023.5	0
0.69~0.76H	2.1	-1101.7	0.002	3.1	-1103.0	0.003	5.4	-1096.0	0.005
0.76~0.83H	9.5	-1011.3	0.009	18.4	-1014.8	0.018	32.9	-1007.8	0.033
0.83~0.90H	42.6	-1020.8	0.042	85.0	-1026.5	0.083	157.3	-1018.6	0.154
0.90~1.00H	1264.1	-1081.9	1.168	2265.8	-1091.0	2.077	3955.7	-1082.2	3.655

Table 6 Eigenvalues of wind and rain loads on internal surface at different heights from conditions 4 to 6

Height	23.7m/s+64mm/h			23.7m/s+100mm/h			23.7m/s+200mm/h		
	Rain load (N)	Wind load (kN)	Ratio (‰)	Rain load (N)	Wind load (kN)	Ratio (‰)	Rain load (N)	Wind load (kN)	Ratio (‰)
0.00~0.69H	0	-12932.8	0	0	-12856.9	0	0	-13082.5	0
0.69~0.76H	1.7	-1655.1	0.001	4.9	-1597.8	0.003	12.1	-1614.9	0.007
0.76~0.83H	13.7	-1519.7	0.009	19.8	-1469.8	0.013	40.6	-1485.4	0.027
0.83~0.90H	26.7	-1533.0	0.017	50.0	-1485.2	0.034	80.3	-1501.6	0.053
0.90~1.00H	845.1	-1629.3	0.519	1325.3	-1584.1	0.837	2781.0	-1601.9	1.736

Table 7 Eigenvalues of wind and rain load on internal surface at different heights from conditions 7 to 9

Height	25.3m/s+64mm/h			25.3m/s+100mm/h			25.3m/s+200mm/h		
	Rain load (N)	Wind load (kN)	Ratio (‰)	Rain load (N)	Wind load (kN)	Ratio (‰)	Rain load (N)	Wind load (kN)	Ratio (‰)
0.00~0.69H	0	-15368.8	0	0	-14985.9	0	0	-15297.4	0
0.69~0.76H	2.6	-1782.3	0.001	4.1	-1868.8	0.002	7.1	-1723.9	0.004
0.76~0.83H	10.5	-1640.1	0.006	17.6	-1714.7	0.010	25.0	-1582.2	0.016
0.83~0.90H	38.6	-1663.4	0.023	63.0	-1734.0	0.036	104.2	-1600.8	0.065
0.90~1.00H	726.9	-1777.1	0.409	1539.8	-1846.8	0.834	2693.1	-1706.6	1.578

As shown in Tables 5-7, the rain loads are mainly concentrated on the internal surface at the height of 0.69H-1.0H. To clearly indicate the position and number of raindrops at each height and the corresponding pressure coefficient, the 3D distribution of the rain-induced internal pressure coefficient is given in Fig. 12. The coordinate system of the wind/rain field is rotated counterclockwise by 90° with coarsening of raindrops to show the positions hit by raindrops. Comparison would reveal the following:

(1) The leeward region in the upper part of the internal surface of the tower is hit more frequently by the raindrops under different working conditions. Driven by airflow vortex inside the tower, only a few raindrops are collected in the windward region. The largest number of raindrops is collected on the internal surface under working condition 3. As the wind velocity increases, the number of raindrops collected decreases; but it increases along with the increase in rainfall intensity.

(2) Rain-induced internal pressure coefficient under each working condition is concentrated within the range of 0.9H-1.0H in the meridional direction and 60°-300° in the circumferential direction. The values are generally very small or zero in other positions. The maximum is 0.0038 found at the height of 0.90-1.0H under working condition 3.

This finding is consistent with the above analysis.

Four representative cross sections are selected in the upper part of the tower body and the equivalent internal pressure coefficients are compared under nine working conditions, as shown in Fig. 13.

(1) The distribution of the internal pressure coefficient shows a significant 3D effect. The equivalent internal pressure coefficients of four representative cross sections are different under each working condition. However, the values are basically symmetrical about the wind axis.

(2) The circumferential distributions of equivalent internal pressure coefficient are basically consistent under different working conditions, though the values are somewhat different. The minimum and maximum values on each curve of the cross section are generally enveloped by working condition 9 in pink and working condition 4 in blue, respectively.

(3) The absolute values of equivalent internal pressure coefficients on each cross section decrease in the leeward regions (indicated by the blue dashed line box). This is because the airflow passes through the shutters and hits the internal surface of the leeward region; moreover, the raindrops hit the upper internal surface due to the incoming wind. The airflow has a greater impact on the internal pressure coefficient than the raindrops.

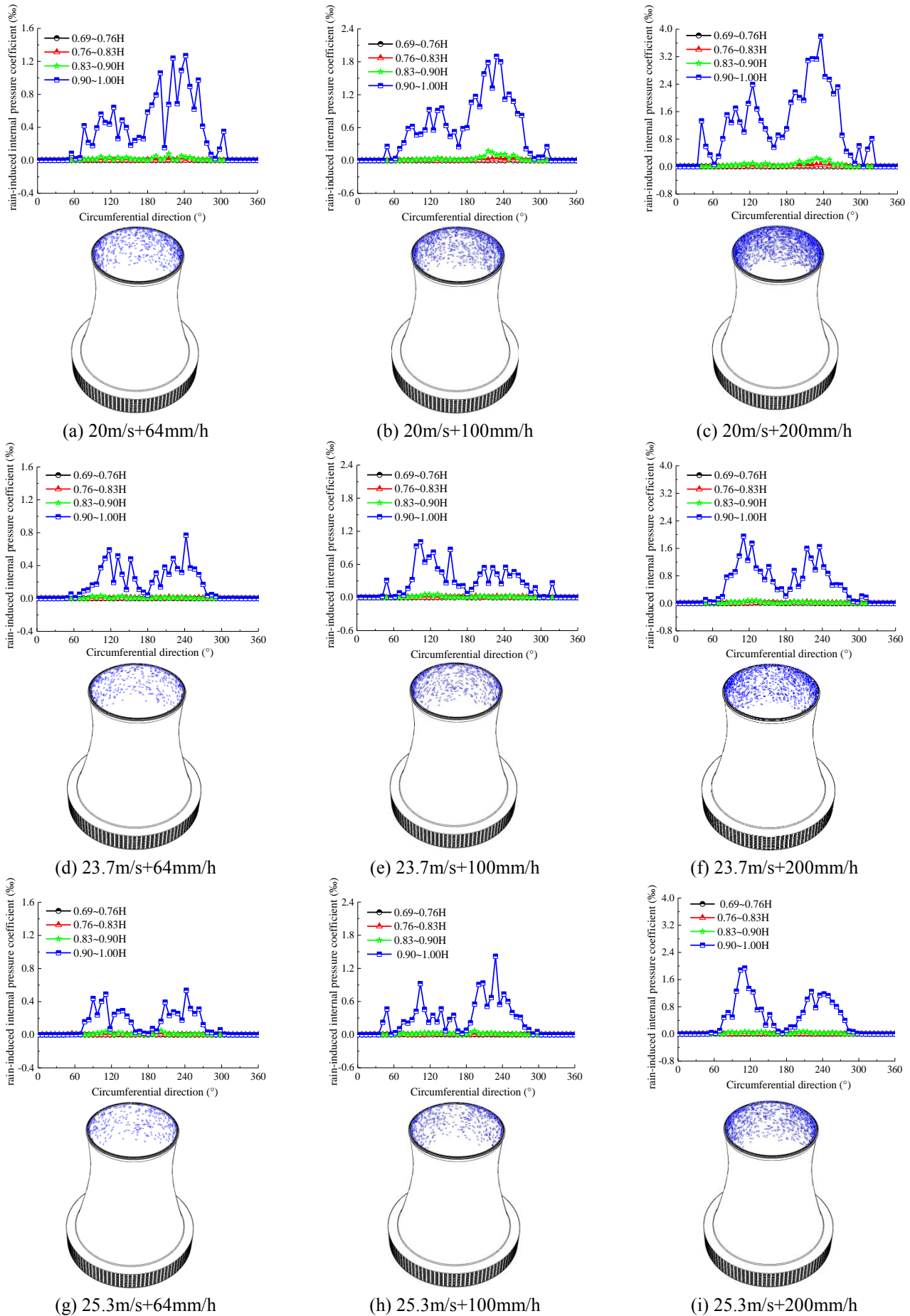


Fig. 12 3D distribution of rain-induced internal pressure coefficient on internal surface under each working condition

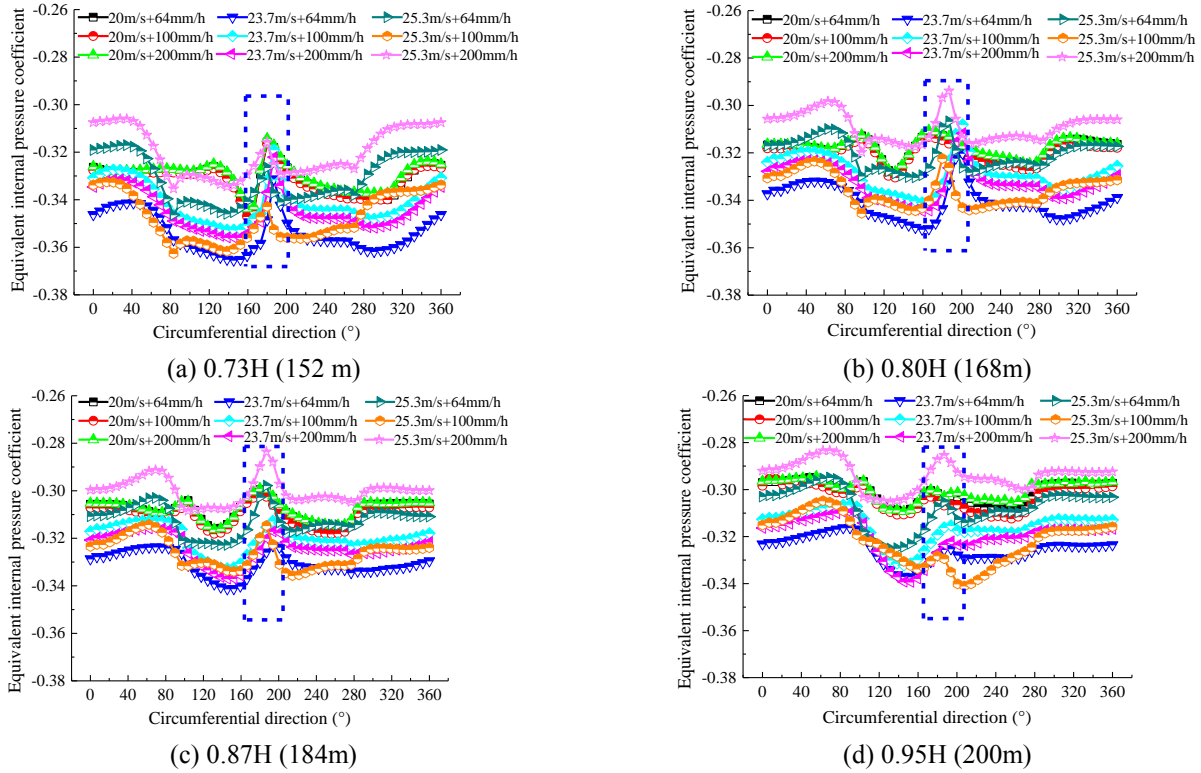


Fig. 13 Comparison of circumferential equivalent internal pressure coefficient over representative cross-sections of the cooling tower

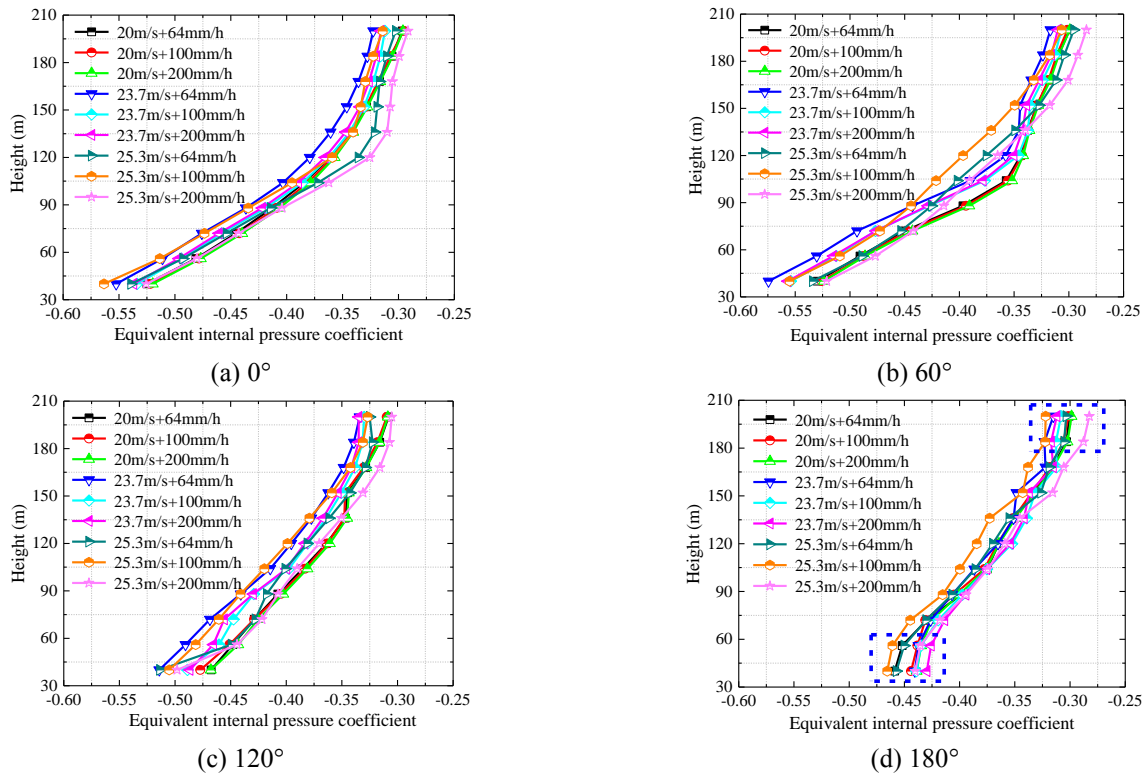


Fig. 14 Comparison of meridional equivalent internal pressure coefficients under 9 working conditions

Based on the circumferential distribution of equivalent internal pressure coefficient, four meridians (0° , 60° , 120° and 180°) are chosen to further compare the equivalent internal pressure coefficient under nine working conditions.

It can be seen from Fig. 14 that the distribution pattern of internal pressure coefficient is basically consistent under different meridional angles. The absolute values decrease with height. The maximum is -0.574 and the minimum is -

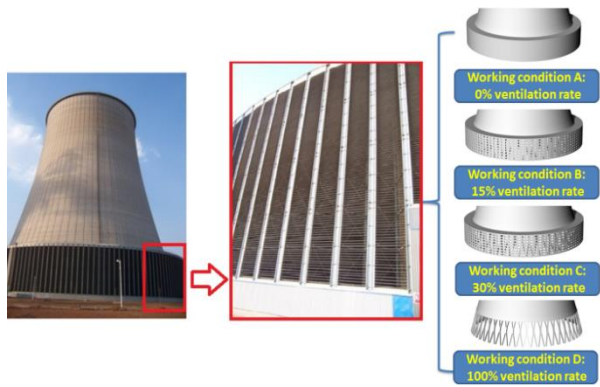


Fig. 15 Computational model under four ventilation rates

0.282. Compared with other angles, the absolute values of equivalent internal pressure coefficient at the bottom of the internal surface decreases significantly under 180° . In contrast, the absolute values of equivalent internal pressure coefficient at the top decreases only mildly.

6. Influence of ventilation rate of shutters

Ventilation rate of shutters has a significant impact on the airflow and raindrop movements inside the cooling tower. The influence of ventilation rate on internal pressure of cooling tower is discussed under the most unfavorable working condition, i.e., working condition 3, which is the combination of wind velocity 20m/s + rainfall intensity 200mm/h . The ventilation rate of shutters around the cooling tower is related to the construction stage and operational status (Ke *et al.* 2015). Four ventilation rates are considered: (1) construction stage: ventilation rate of 100%; (2) operational stage: ventilation rate of 15% and 30% under the design wind speed; (3) operational stage: ventilation rate of 0% when the shutters are completely closed during winter to prevent freezing.

The four ventilation rates (0%, 15%, 30% and 100%) correspond to working condition A, B, C and D, respectively. The computational model is shown in Fig. 15.

6.1 Influence of ventilation rate on wind field

Figs. 16-17 are the 3D wind velocity streamlines and distribution of turbulence kinetic energy under the four working conditions before considering the effect of raindrops. Comparison indicates that:

(1) As the ventilation rate increases, an unobstructed wind channel is formed inside the cooling tower. The airflow accumulates less intensively, and the flow lines become sparse. There is a greater amount of airflow entering the tower via the air inlet under complete ventilation. When this part of airflow collides with the airflow entering from the tower top, the flow lines become denser in the middle of the tower. Input and output take place at both the tower base and tower top, which enhances the convection and the vortex shedding phenomenon.

(2) Turbulence kinetic energy on windward side of the top of tower and leeward side of the middle of tower first

decreases and then increases with the increase of ventilation rate. The turbulence kinetic energy is lower at the air outlet and in the leeward region under working condition C. The turbulence kinetic energy at the tower base is the smallest under working condition A; it is the highest under working condition B, followed by working condition C and D successively. Part of the turbulence kinetic energy under working condition D is concentrated in the leeward region inside the tower.

6.2 Influence of ventilation rate on rain field

Fig. 18 shows the raindrop trajectories in the coupled wind and rain fields under the four working conditions. The density of the raindrops is subjected to proportional coarsening. It can be seen that a large number of raindrops separate and move towards the two sides of the tower along the wall surface under the action of wind. Only part of the raindrops hit the windward region. The airflow at the tower top drives the majority of the raindrops to slide over the top and go into the wake zone; only a small portion of the raindrops enter the tower. As the ventilation rate increases, the raindrop velocity increases in the crosswind region of the tower. Raindrops in the lower part of the tower enter the tower via the shutters. This phenomenon is even more significant under the ventilation rate of 100%.

Fig. 19 is the comparison of number, impact velocity and occupancy of velocity of raindrops with different diameters under the four working conditions. It can be seen that:

(1) The diameters of raindrops captured by the internal wall surface under different ventilation rates vary from 3 to 6mm, and raindrops with a diameter of 5mm account for the largest proportion. This is because the velocity of smaller raindrops increases more quickly under the same wind force.

(2) The distribution of occupancy and values of horizontal raindrop velocity is basically consistent under different working conditions. The impact velocity of the raindrops varies from 0 to 5m/s , and the maximum occupancy is 98.97%, which occurs under working condition B.

(3) The mean horizontal velocities of raindrops hitting the internal surface are far smaller than the baseline velocities under different working conditions. The values vary from 1 to 3m/s . The impact velocity increases as the raindrop becomes larger in size.

6.3 Influence of ventilation rate on equivalent internal pressure

Fig. 20 shows the 3D distribution of wind-induced internal pressure coefficient under different ventilation rates of the shutters. It can be seen that the values along the circumferential and meridional directions are different under different working conditions. But they are generally symmetrical about the wind axis. As the ventilation rate increases, the airflow passing through the shutters has a greater influence on the internal surface at the bottom of the tower. The wind-induced internal pressure coefficient at the bottom of the tower jumps more violently along the circumferential direction. Its absolute value decreases

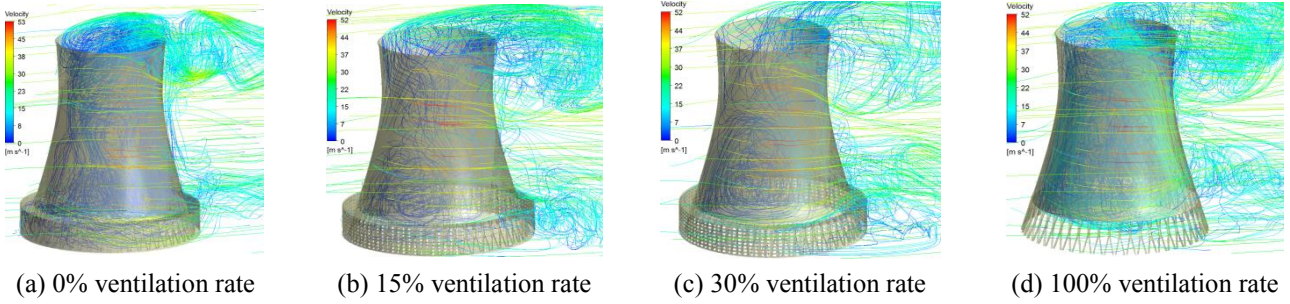


Fig. 16 3D Wind velocity streamlines under four ventilation rates

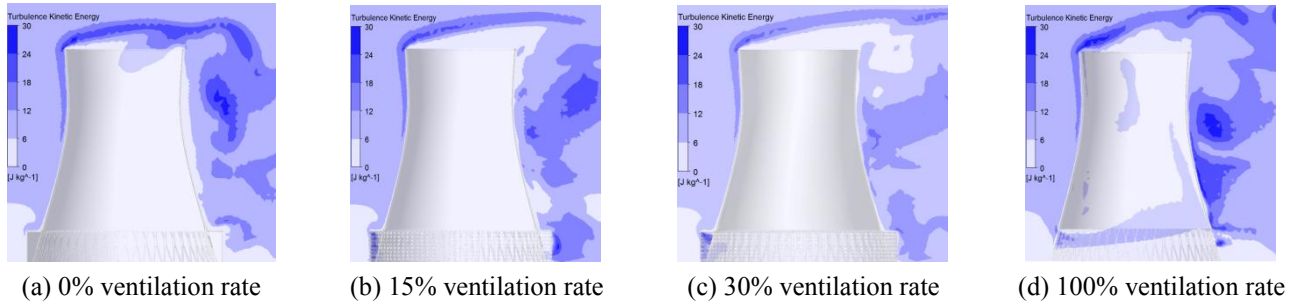


Fig. 17 Turbulence kinetic energy under four ventilation rates

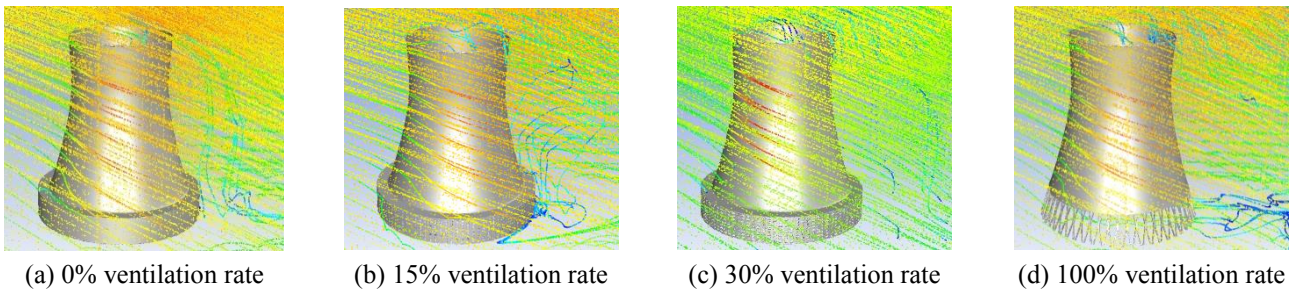


Fig. 18 Raindrop trajectories in the coupled wind and rain fields under four ventilation rates

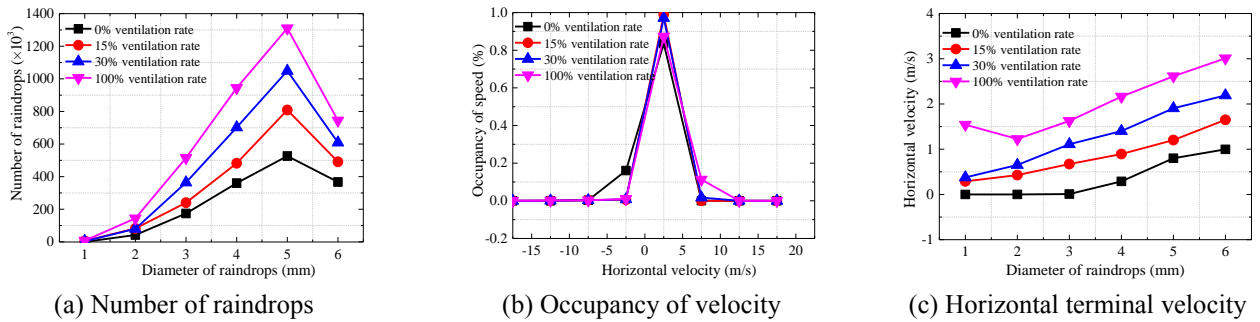


Fig. 19 Number of raindrops with different diameter and horizontal terminal velocity of raindrops under four ventilation rates

gradually in the leeward region at the bottom of the tower. Positive pressure even occurs in some positions under working condition D.

Tables 8-9 are comparison of the ratios of rain to wind loads on the internal surface of the tower body under different heights (H is the tower height 210m). It can be seen that the rain load on the internal surface increases with height, regardless of the working condition. No raindrops are collected on the internal surface below 0.69H (145m), and the majority of the rain load is concentrated at the height of 0.90-1.0H (189-210m), accounting for over 90%.

The ratios of rain to wind load are extremely small at each height, and the maximum is only 7.65%, which occurs at the height of 0.90-1.0H under working condition D. Except for some positions that are subjected to considerable wind-induced turbulence effect, the overall rain load and the local rain load at the cross section of equal height increase with the increase of the ventilation rate.

Fig. 21 shows the 3D distribution of rain-induced internal pressure coefficient under each working condition. To more clearly visualize the positions hit by the raindrops, the coordinate system of the wind/rain field is rotated

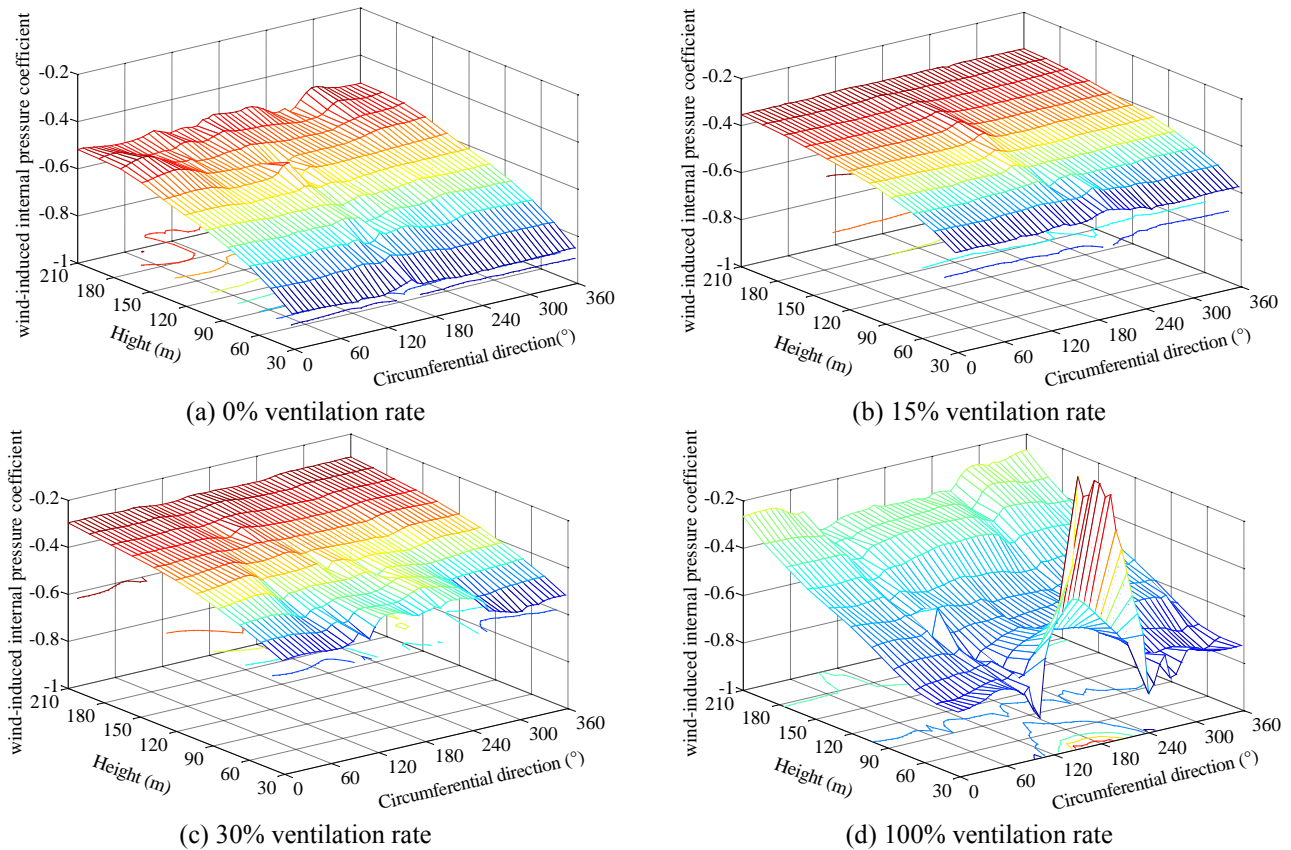


Fig. 20 3D distribution of wind-induced internal pressure coefficient under different working conditions

Table 8 Eigenvalues of wind and rain load on internal surface at different heights under working condition A and B

Height	0% ventilation rate			15% ventilation rate		
	Rain load (N)	Wind load (kN)	Ratio (‰)	Rain load (N)	Wind load (kN)	Ratio (‰)
0.00~0.69H	0	-15155.8	0	0	-10106.2	0
0.69~0.76H	6.9	-1892.7	0.004	1.8	-1264.8	0.001
0.76~0.83H	22.9	-1746.1	0.013	12.6	-1169.5	0.011
0.83~0.90H	38.4	-1780.2	0.022	52.0	-1185.9	0.044
0.90~1.00H	805.9	-1882.1	0.428	1873.3	-1260.9	1.486

Table 9 Eigenvalues of wind and rain load on internal surface at different heights under working condition C and D

Height	30% ventilation rate			100% ventilation rate		
	Rain load (N)	Wind load (kN)	Ratio (‰)	Rain load (N)	Wind load (kN)	Ratio (‰)
0.00~0.69H	0	-9023.5	0	0	-12892.7	0
0.69~0.76H	5.4	-1096.0	0.005	58.7	-1479.2	0.040
0.76~0.83H	32.9	-1007.8	0.033	150.0	-1245.7	0.120
0.83~0.90H	157.3	-1018.6	0.154	671.7	-1198.4	0.560
0.90~1.00H	3955.7	-1082.2	3.655	8971.3	-1172.8	7.650

counterclockwise with coarsening of the raindrops. It can be seen from the figure that

(1) The leeward region in the upper internal surface of the tower is most frequently hit by the raindrops under different working conditions. Driven by the airflow vortices inside the tower, only a few raindrops are collected in the windward region of the internal surface. The number of raindrops collected on the internal surface increases with the ventilation rate. Under working condition D where the ventilation rate is 100%, the number of raindrops collected in the upper leeward region is significantly lower than that in the cross-wind region.

(2) The rain-induced internal pressure coefficients under each working condition are generally found at the height of 0.9H~1.0H and at the circumferential angle of 60°~300°.

The values of rain-induced internal pressure coefficient are very small, and the maximum is only 0.013 and found at the height of 0.90~1.0H under working condition D.

Fig. 22 is the comparison of circumferential equivalent internal pressure coefficients on four representative cross sections in the upper part of the tower body. It can be seen that different ventilation rates of the shutters have a significant influence on the equivalent internal pressure coefficient. The circumferential distribution of equivalent internal pressure coefficient is different at different cross sections, and the values are basically symmetrical about the wind axis. Except for working condition D that is subjected to considerable interference from airflow vortices, the minimum and maximum values at each cross section under the other three working conditions are enveloped by

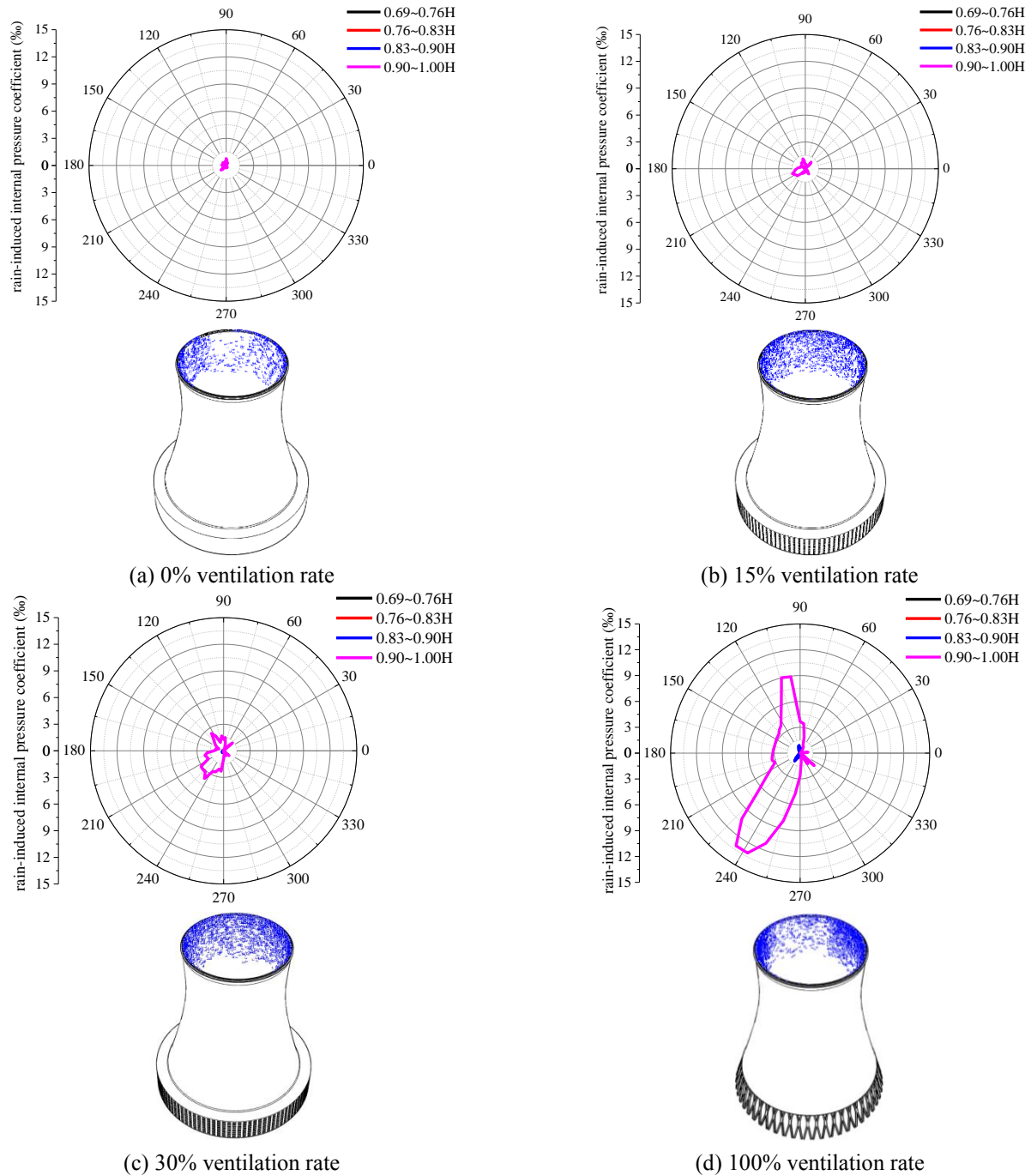


Fig. 21 3D distribution of rain-induced internal pressure coefficient under different working conditions

working condition C in blue and working condition A in green, respectively. The absolute values of equivalent internal pressure coefficient is the highest under working condition A, followed by working condition B and C successively.

Based on the above analysis, meridional equivalent internal pressure coefficients are compared along four representative meridians (0° , 60° , 120° and 180°), as shown in Fig. 23. It can be seen that the distribution patterns of meridional equivalent internal pressure coefficient are basically consistent under working conditions A to C. The absolute values decrease at higher height under different

working conditions. The maximum is -0.864 and found at the bottom of the tower under working condition A. When the ventilation rate is 100%, a larger amount of airflow enters the tower body and exhibits complex movement pattern. Airflow vortices moving at a high speed cause a jump in local pressure at the bottom of the tower, and the absolute values of equivalent internal pressure coefficient decreases dramatically.

Based on the above analysis, the tower body is divided into four regions along the circumferential and meridional directions, respectively. Values of equivalent internal pressure coefficients are given for each region under

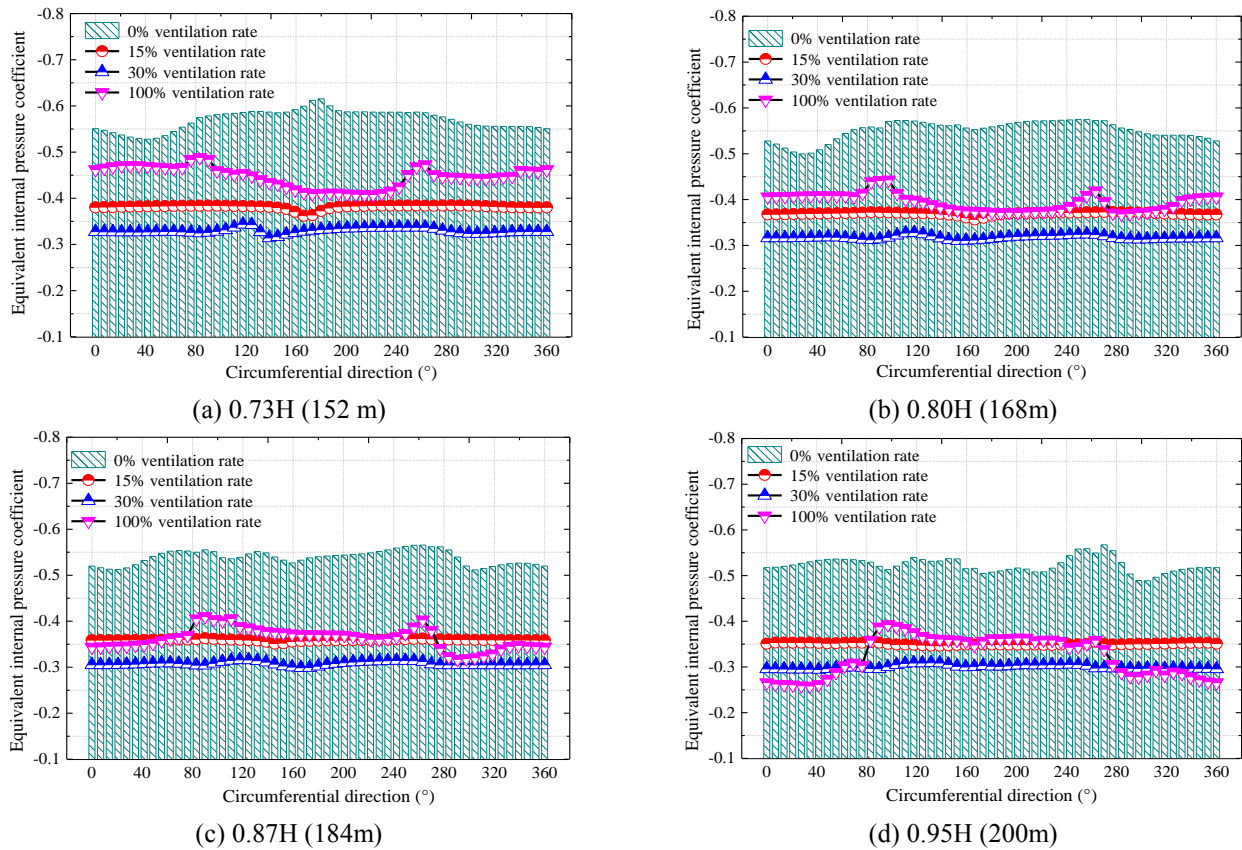


Fig. 22 Comparison of circumferential equivalent internal pressure coefficients over representative cross sections under four ventilation rates

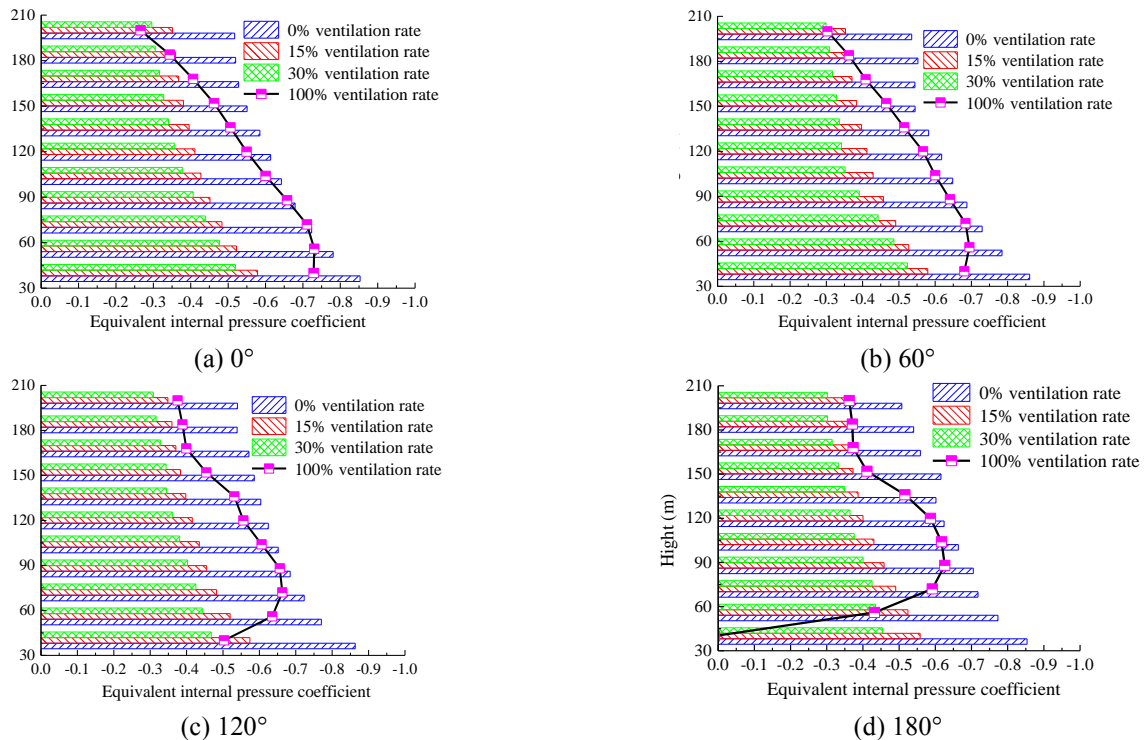


Fig. 23 Comparison of equivalent internal pressure coefficients along representative meridian lines under four ventilation rates

different ventilation rates, as shown in Fig. 24. Thus the values of equivalent internal pressure coefficients can be

directly used for different regions of the cooling tower during structural design.

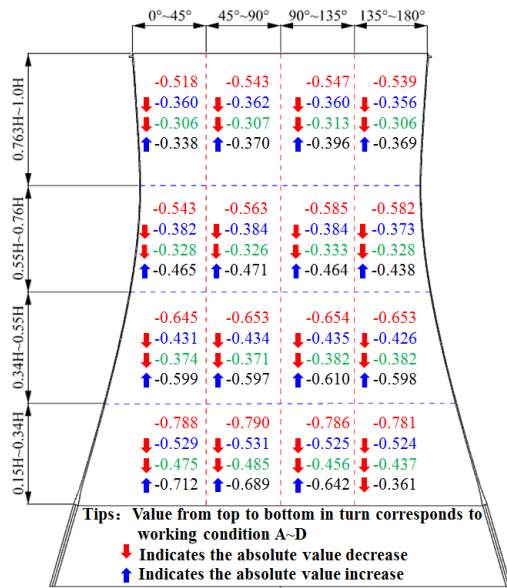


Fig. 24 Values of equivalent internal pressure coefficient for different regions of the tower under four ventilation rates

Apparently, the equivalent internal pressure coefficient in the leeward region at the bottom of the tower undergoes a jump. The absolute values in other regions first decreases and then increases with the increase in the ventilation rate. The absolute values are the smallest under 30% ventilation rate, and they decrease at a higher height under each working condition. The absolute values in the circumferential range of 135°-180° are the smallest.

7. Conclusions

The aerodynamic performance and working mechanism of internal pressures in super-large cooling tower under two-way coupling between strong wind and heavy rain are discussed in this study. Different combinations of wind velocity and rainfall intensity are considered along with four different ventilation rates of the shutters. The wind field and rain field are simulated iteratively using continuous and discrete phase models, respectively. The following conclusions are drawn:

- Raindrops are subjected to greater horizontal force as wind velocity increases. This propels the raindrops at an acceleration speed. Due to the driving and enveloping effect at the front edge of the cooling tower and the airflow coming out of the tower, a large number of raindrops slide over the tower top and enter the wake zone. Only a small portion of raindrops enter the tower, collide with the airflow and hit the internal surface of the tower.
- The regions hit by raindrops under different working conditions are generally the leeward regions in the upper internal surface of the tower. The occupancy of diameter of 5mm and impact velocity of 1-3m/s is the highest. The number of raindrops accumulating on the internal surface decreases as the wind velocity increases, but increases with the increase of rain fall intensity. The number of raindrops

collected on the internal surface increases with the increase in the ventilation rate of shutters.

- The load imposed by raindrops on the internal surface and the rain-induced internal pressure coefficient are very small. The maximum ratio of rain load to wind load is only 7.65%. The maximum rain-induced internal pressure coefficient is 0.013 and found at 0.90-1.0H under the wind velocity of 20m/s, rainfall intensity of 200mm/h and 100% ventilation rate.

- The equivalent internal pressure coefficient undergoes a jump in the leeward region at the bottom of the tower. In other regions, the absolute values of equivalent internal pressure coefficient first decreases and then increases with the increase in the ventilation rate. The absolute value is the smallest under 30% ventilation rate. Moreover, all absolute values of equivalent internal pressure coefficients decrease at a higher height regardless of the working condition. The absolute values are the smallest in the circumferential range of 135°-180°, as compared with other intervals.

Acknowledgments

The research described in this paper was financially supported by the National Natural Science Foundation (51878351, U1733129 and 51761165022), Jiangsu Province Outstanding Natural Science Foundation (BK20160083), Jiangsu qinglan Project and Postdoctoral Science Foundation (2013M530255; 1202006B).

References

- ANSYS (2011), Ansys Fluent Theory Guide, ANSYS Inc., PA, USA.
- Bennett, M., Kodakalla, V. and Gupta, V. (2011), "Vibration mitigation measures in cable stayed bridges", *J. Molecular Struct.*, **996**(1-3), 64-68.
- Blocken, B., Dezsö, G., Beeck, J.V. and Carmeliet, J. (2010), "Comparison of calculation models for wind-driven rain deposition on building facades", *Atmospheric Environ.*, **44**(14), 1714-1725. <https://doi.org/10.1016/j.atmosenv.2010.02.011>.
- Chen, B.W. (2009), "Numerical simulation of wind and rain pressure on low building surface", Postgraduate Dissertation, Harbin Institute of Technology, Harbin.
- Chen, X., Zhao, L., Cao, S.Y. and Ge, Y.J. (2016), "Extreme wind loads on super-large cooling towers", *J. Int. Assoc. Shell Spatial Struct.*, **57**(1), 49-58. <https://doi.org/10.20898/j.iass.2016.187.772>.
- DL/T 5339-2006 (2006), Code for hydraulic design of fossil fuel power plants, The Ministry of Construction of China; Beijing, China.
- Douvi, E. and Margaritis, D. (2012), "Aerodynamic performance investigation under the influence of heavy rain of a NACA 0012 airfoil for wind turbine applications", *Int. Rev. Mech. Eng.*, **6**(6), 1-8.
- Fu, X., Li, H.N. and Li, G. (2016), "Fragility analysis and estimation of collapse status for transmission tower subjected to wind and rain loads", *Struct. Safety*, **58**, 1-10. <https://doi.org/10.1016/j.strusafe.2015.08.002>.
- GB 50009-2012 (2012), Load code for the design of building structures, The Ministry of Structure of the People's Republic of China; Beijing, China.

- GB/T 50102-2014 (2014), Code for design of cooling for industrial recirculating water, The Ministry of Construction of China; Beijing, China.
- Goudarzi, M.A. and Sabbagh-Yazdi, S.R. (2011), "Effects of modeling strategy on computational wind pressure distribution around the cooling towers", *Wind Struct.*, **14**(1), 81-84.
- Gunn, R. and Kinzer, G.D. (1949), "The terminal fall velocity for water droplets in stagnant air", *J. Atmospheric Sci.*, **6**(4), 243-248.
- Hodson, M.C. (1986), "Raindrop size distribution", *J. Appl. Meteorology*, **25**(7), 1070-1074.
- Jiang, F. (2008), *Fluent Advanced Application And Case Analysis*, Tsinghua University Press, Beijing, China.
- Ke, S.T. and Ge, Y.J. (2014), "The influence of self-excited forces on wind loads and wind effects for super-large cooling towers", *J. Wind Eng. Industrial Aerodynam.*, **132**, 125-135. <https://doi.org/10.1016/j.jweia.2014.07.003>.
- Ke, S.T., Ge, Y.J., Zhao, L. and Tamura, Y. (2015), "Stability and reinforcement analysis of super large exhaust cooling towers based on a wind tunnel test", *J. Struct. Eng.*, **141**(12), 04015066.
- Ke, S.T., Liang, J., Zhao, L. and Ge, Y.J. (2015), "Influence of ventilation rate on the aerodynamic interference for two IDCs by CFD", *Wind Struct.*, **20**(3), 449-468. <https://doi.org/10.12989/was.2015.20.3.449>.
- Ke, S.T., Du, L.Y. and Hou, X.A. (2018), "Study on the absorption wind vibration coefficient of super-large cooling tower considering the ventilation rate of Venetian blinds", *J. Building Struct.*, **39**(8), 36-44.
- Liu, S., Huang, S.H. and Li, Q.S. (2017), "3D numerical simulation of wind-driven rain on bridge deck sections based on eulerian multiphase model", *Eng. Mech.*, **34**(4), 63-71.
- Li, H.N. and Bai, H.F. (2008), "Study on wind (rain) induced vibration response and stability of transmission tower system", *China Civil Eng. J.*, **41**(11), 31-38.
- Marshall, J.S. and Palmer, W.M. (1948), "The distribution of raindrops with size", *J. Meteorology*, **5**(4), 165-166. <https://doi.org/10.1002/qj.49707632704>.
- Mcfarquhar, G.M. and List, R. (2010), "The raindrop mean free path and collision rate dependence on rainrate for three-peak equilibrium and Marshall-Palmer distributions", *J. Atmospheric Sci.*, **48**(48), 1999-2004.
- Mcfarquhar, G.M. (2016), "Raindrop size distribution and evolution", *Geophysical Monograph*, **191**, 49-60.
- Niemann, H.J. and Kopper, H.D. (1998), "Influence of adjacent buildings on wind effects on cooling towers", *Eng. Struct.*, **20**(10), 874-880.
- Rigby, E.C., Marshall, J.S. and Hirschfeld, W. (2010), "The development of the size distribution of raindrops during their fall", *J. Atmospheric Sci.*, **11**(5), 362-372.
- Shen, G.H., Zhang, C.S. and Sun, B.N. (2011), "Numerical simulation of wind load on inner surface of large hyperbolic cooling tower", *J. Harbin Institute of Technol.*, **43**(4), 104-108.
- Sun, T.F. and Zhou, L.M. (1983), "Without ribs the elliptic wind pressure distribution of the cooling tower full size measurement and wind tunnel study", *J. Air Dynam.*, **12**(4), 12-17.
- VGB-R610Ue (2005), *VGB-Guideline: Structural Design of Cooling Tower - Technical Guideline for the Structural Design, Computation and Execution of Cooling Towers*, VGB Power Tech, Essen, Germany.
- Wang, L.Y. and Xu, Y.L. (2010), "Active stiffness control of wind-rain-induced vibration of prototype stay cable", *Int. J. Numerical Methods Eng.*, **74**(1), 80-100. <https://doi.org/10.1002/nme.2152>.
- Wang, Z.Y., Zhao, Y., Li, F.Q. and Jiang, J.Q. (2013), "Extreme dynamic responses of mw-level wind turbine tower in the strong typhoon considering wind-rain loads", *Math. Problems Eng.*, **3**, 133-174. <http://doi.org/10.1155/2013/512530>.
- Wu, J.K. (1996), "Review and prospect of structural analysis of large cooling towers", *Mech. Practices*, **18**(6), 1-5.
- Xin, D.B., Zhang, M.J., Wang, L., Ou, J.P. and Li, H. (2011), "Experimental study on wind-induced vortex-induced vibration of girders of long-span Bridges", *J. Harbin Eng. U.*, **32**(9), 1168-1172.
- Xin, D.B., Li, H., Wang, L. and Ou, J.P. (2012), "Experimental study on static characteristics of the bridge deck section under simultaneous actions of wind and rain", *J. Wind Eng. Industrial Aerodynam.*, **s**(107-108), 17-27. <https://doi.org/10.1016/j.jweia.2012.03.002>.
- Yang, J.T. and Lou, W.J. (2011), "CFD simulation of wind-driven rain and calculation method of average rain load", *Acta Aerodynamica Sinica*, **29**(5), 600-606.
- Zou, Y.F., Niu, H.W. and Chen, Z.Q. (2015), "Three-dimensional effect of wind load on the single tower of the special large cooling tower, and its design value", *J. Hunan U.*, **32**(1), 76-82.
- Zhang, Q.C. (2010), "Static bifurcation of rain-wind-induced vibration of stay cable", *Acta Physica Sinica*, **59**(2), 729-734.
- Zhang, J.F., Ge, Y.J. and Zhao, L. (2013), "Influence of latitude wind pressure distribution on the responses of hyperboloidal cooling tower shell", *Wind Struct.*, **16**(6), 579-601. <http://dx.doi.org/10.12989/was.2013.16.6.579>.

CC